sciendo

ANNALS OF WEST UNIVERSITY OF TIMISOARA PHYSICS
Vol. LXIV, 2022

DOI : 10.2478/awutp-2022-0009

INVESTIGATION OF THE OPTOELECTRONIC AND PHOTOVOLTAIC PROPERTIES OF $Y_XIN_{1-X}P$ ALLOYS USING FIRST PRINCIPLES CALCULATIONS

Khedija Talbi[1], Youcef Cherchab[1,2], Ali Mir[1], Bachir Bouhadef[1]

[1]*Department of Physics, University of Relizane, Ahmed Zabana, Bormadia, Relizane 048000, Algeria.*
[2] *Laboratoire de Microphysique et de Nanophysique (LaMiN), ENPO (ex : ENSET-Oran), BP 1523 EL M'Naouer, Oran 31000, Algeria.*
*Corresponding author: Email: cherchab@gmail.com

Article Info

Received: 20.09.2022
Accepted: 08.11.2022

Keywords:
DFT, FP-LAPW, Doping, structural stability, phase transition, optoelectronic properties, photovoltaic properties

Abstract

Structural stability, electronic, optical, and photovoltaic properties of pure and doped InP were evaluated by using first principles calculations via the density functional theory (DFT). The exchange-correlation potential is treated with generalized gradient approximation (GGA-PBE). Additionally, the Tran Blaha modified Becke-Johnson exchange potential (TB-mBJ) is employed, because it gives very accurate results of the band gap in solids. Our results reveal that all compounds are energetically and mechanically stable. It is found that for Y concentrations less than 30%, the favored structure is a Zinc blende-like one, while for Y concentrations greater than 30%, the favored structure is a NaCl-like structure. The substitution of In by Y is found to be able to enlarge the direct bandgap of about 34% (from 1.43 eV to 2.17 eV) and confirms the semiconductor behavior for zinc blende stable structures. The absorption coefficient is reasonably exceeding $10^5 cm^{-1}$ for YxIn1-xP alloys in the case (x=0 and x=25%). The reflectivity shows less than 30% around the energy value of 2 eV and an efficiency of solar cell of 18% can be achieved for Y0.25In0.75P. Also, a thickness of $L = 1\mu m$ is enough to confirm the experimental data. Regarding to the matching of lattice parameters (a mismatch $< 4\%$) of InP and Y0.25In0.75P and the band gap energy difference made Y0.25In0.75P suitable for optoelectronic and photovoltaic devices in particularity as Tandem solar cells (Y0.25In0.75P/InP) and quantum well (Y0.25In0.75P/InP/Y0.25In0.75P) applications. In the absence of experimental works, our results can be useful for further studies.

1. Introduction

Transition-metal phosphide (TMP) ternary alloys are attractive in the field of optoelectronic applications [1-4] and received increased attention over the last few years. Progress in the optoelectronic for TMP ternary alloys due to the efforts have been devoted experimentally, Henkes et al. [5] used a new strategy for synthesizing nanostructures of a

variety of 3d, 4d, and 5d transition-metal phosphide with no condition of adjustable parameters such as the size, shape, chemical composition and segregation effects, allow a large investigation of TMP ternary alloys. In the literature, an extensive exploration of TMP ternary alloys is reported in experimental and theoretical studies [6-17]. $In_xAl_{1-x}P$ and $Ga_xAs_{1-x}P$ alloys [18],[19] show a bandgap engineering with the turn off the nature of bandgap from indirect to direct, the results of $Sc_{1-x}In_xP$ alloys [20] provides that changing of direct bandgap from X point to Γ point. The work reported by Lopez et al. [21] shows that $Sc_xY_{1-x}P$ alloys operate at high temperatures applications. A similar trend was inspected in the nitride III-V ternary alloys such as ScGaN, ScAlN, and YGaN alloys [22], [23]. In fact, the replacement of Indium (In) by Scandium (Yttrium) Sc (Y) atoms leads to an efficient way to enhance the potential of ScGaN, and YGaN alloys in high-temperature applications rather than the well-known InGaN alloy [23], [24].

On the same footing, we have combined Y with InP, which exhibits different physical properties, to obtain new materials of $Y_xIn_{1-x}P$ alloys. InP is a very popular semiconductor in optoelectronic devices [25], [26], crystallizes in the Zinc blende (B3) lattice, which undergoes a pressure transition to Rock-Salt (B1) lattice at 10.8 GPa [27]. The direct bandgap of InP estimated to be 1.423 eV [28]. On the other hand, YP has metallic behavior and shows a covalent character, crystallizes in the Rock-Salt (B1) lattice, and at high pressure transforms to CsCl lattice (B2) at 55.94 GPa [29]. The similarity of physical properties obtained for $Sc_xGa_{1-x}P$, $Sc_xIn_{1-x}P$, and $In_xGa_{1-x}P$ [20], [30], [31], motivated us to study the structural, elastic**,** and electronic properties of $Y_xIn_{1-x}P$ alloys. However, the $Y_xIn_{1-x}P$ alloys have not yet been investigated to our knowledge. The paper is organized as follows: in section 2, we give a brief description of the computational method and parameters used in this work. The obtained results and discussions are given in section 3 and followed by a conclusion.

2. Methodology and computational details

Structural stability, electronic, and optical properties of $Y_xIn_{1-x}P$ alloys have been calculated by self-consisting full potential linearized augmented plane wave (FP-LAPW) method as implemented as the Wien2k package [32] based on density functional theory (DFT) [33]. The exchange-correlation potential was considered within the gradient generation approximation (GGA) [34], to improve the band gaps, we used the modified Beck-Johnson potential (mBJ) [35] which yields a better estimation of band gaps compared to experimental data. We have used muffin-tin radii of 2.1 a.u for Y, 2.5 a.u for In, and 1.9 a.u for P respectively. The parameters of FP-LAPW used in the calculations are $R_{MT}k_{max}$, ℓ_{max} and G_{max}, and are set

to 9, 10, and 14Ry$^{(1/2)}$ respectively. R_{MT} is the smallest atomic sphere radii inside the cell, and k_{max} is a cutoff for the basis function wave vector, ℓ_{max} is the maximum value of augmented momentum of the wave spherical potential and charge density, while G_{max} represents the charge density was Fourier expanded. The Brillouin zone integration is performed with 17x17x17 Monkhost-Pack mesh points [36] for binaries compounds and with 11x11x11 for ternaries compounds. For the electronic self-consistent loop repeated until the energy and the charge convergence. The fulfill parameters are 10^{-5}Ryd and 10^{-3} e^- of energy and charge criteria respectively.

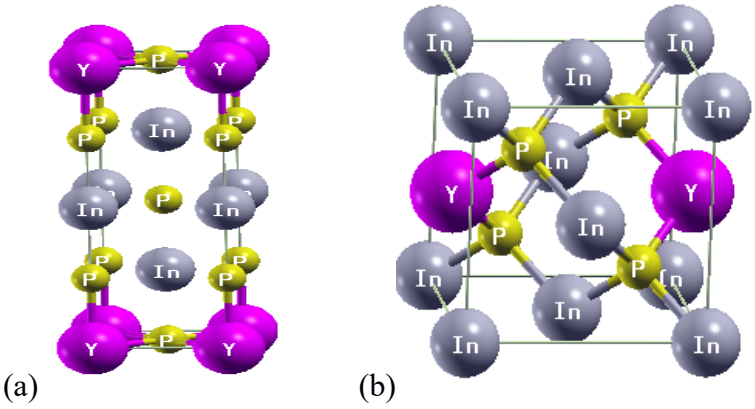


Figure 1. Crystal structure used in our calculations of of $Y_xIn_{1-x}P$ for the concentrations 25% of Y atoms: (a) Rock salt-like structure and (b) Zinc blende-like structure

Figure 1 shows the two configurations of structures used in our calculations. Figure 1a indicates the rocksalt-like structure, we have used a tetragonal geometry as the ordered structure described in term of periodicity repeated supercell random structures (SQSs) [37]. The rocksalt-like structure is deduced from the conventional unit cell of rocksalt structure (B1). Firstly, we obtained the four-tetragonal unit cell with lattice parameters $a = a_0/\sqrt{2}$ and $c = a_0$, where (a, c) is the tetragonal unit sides in the base and along the z-axis respectively. a_0 is the lattice constant of conventional NaCl cell, their space group is P4/mmm (123) with four Wyckoff atomic positions as: 1a (0, 0, 0); 1b (0, 0, 1/2); 1c (1/2, 1/2, 0) and 1d (1/2, 1/2, 1/2). Secondly, by doubling four-tetragonal unit cell along z-direction and finally, we obtained the desired structure containing eight atoms. The second structure is zinc blende-like and is shown in Fig.1b with eight atoms obtained by supercell construction with (1x1x1) configuration. The lattice parameter a equals the lattice parameter of a conventional zinc blende cell (a_0). As shown in Fig.1b in both cases, we replace one, two and three atoms of Indium (In) in order to obtain 25%, 50% and 75% of Yttrium (Y) concentrations. The use of the rock-salt and Zinc

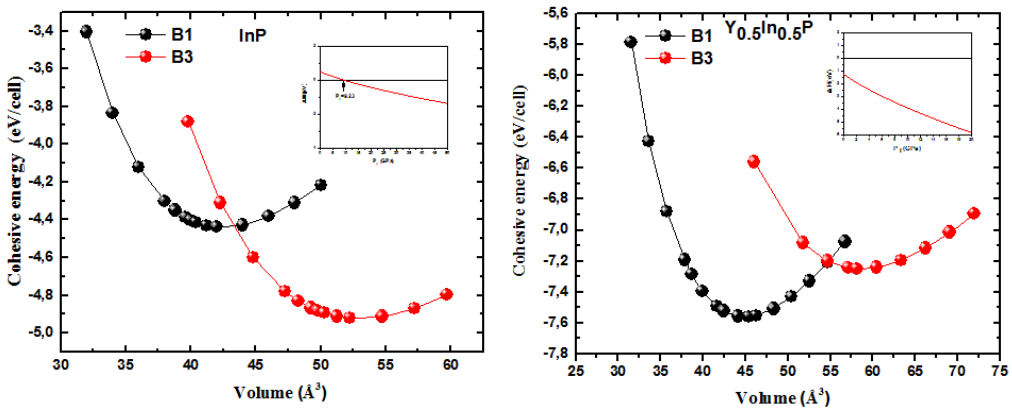
Blende (ZB) terms for ternaries are just in order to refer to the symmetry from which alloy configuration are obtained.

3. Results and discussion

3. 1. Structural Properties

For the binaries, the stability of InP has shown that the ground state structure is zinc blende (B3), which consists of two interpenetrating face centred cubic (fcc) structures displaced from each other by one-quarter of a body diagonal of a unit cell. It can change to the rocksalt (B1) phase under pressure [27] and with a cohesive energy that is higher by 0.48 eV/unit cell [30].

The structure of YP is rock salt (B1), it is suggested that the transform from the rock salt (B1) to zinc Blende (B3) is not possible [38], which the possible ways to reach this structure is by alloying or doping. Therefore, combining InP with YP could result in either zinc blende or rock salt structures. Table 1 summarized the equilibrium results of the lattice constant (a), bulk moduli (B) and energy of cohesion (E_{Coh}) calculated within PBE approximation [39] using the habitual minimization procedure and fit according to the Murnaghan's equation of state [40]. The optimisation of the total energy of $Y_xIn_{1-x}P$ versus volume in both structures of rock salt and zinc blende are shown in Fig. 2. We observe from Table 1 that the lattice parameters for the binaries InP and YP are in agreement with the available data, the YP material has a reasonable mismatch with InP about 2.23% and 5.54% in the NaCl and ZB-like structures respectively, and therefore, the YInP alloy is justified to be combined. In addition, the parameter lattices of $Y_xIn_{1-x}P$ in rock-salt structure are slightly small than in zinc-blende structure, while the bulk modulus is in the opposite order, confirming that $Y_xIn_{1-x}P$ alloys are more rigid in rock-salt structure compared to zinc-blende structure.



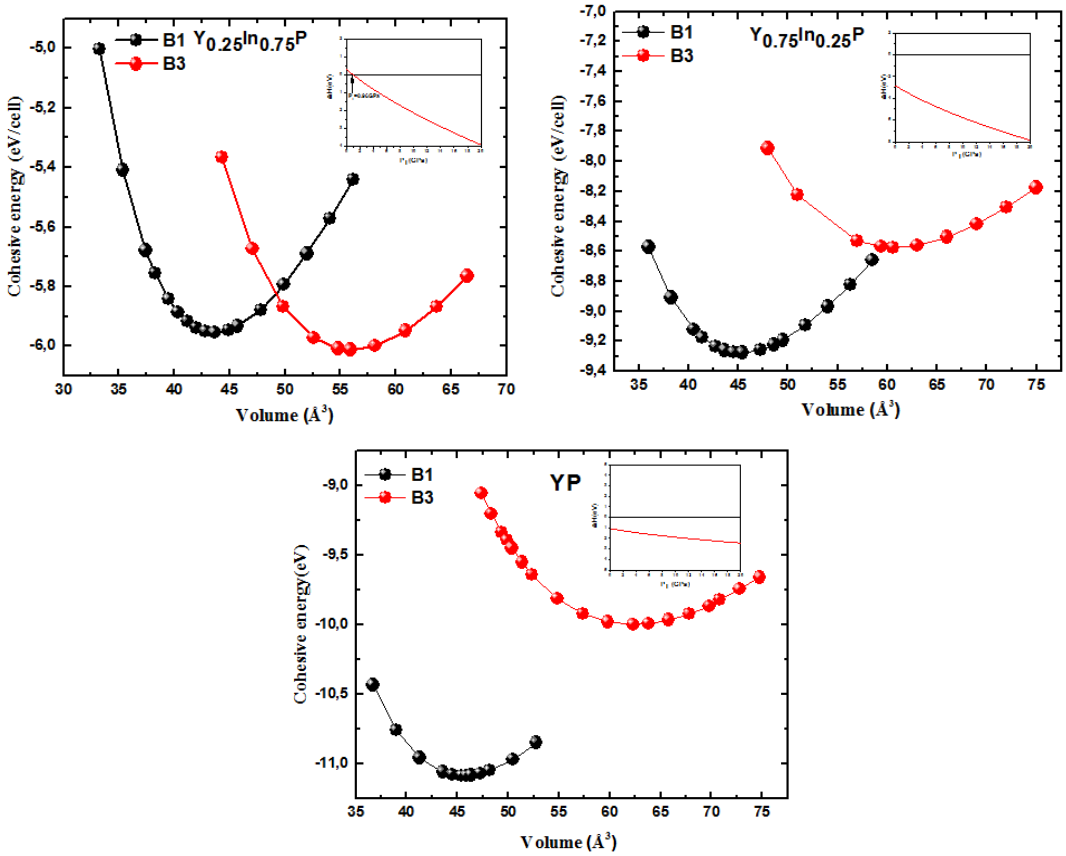


Figure 2. Total energy versus volume for $Y_xIn_{1-x}P$ alloys

Table1. The structural parameters of $Y_xIn_{1-x}P$ in the rocksalt-like structure and ZB structure. Cohesive energies and volumes are given per unit cell (containing 8 atoms). The parameter $a_0(\text{Å})$ in the rocksalt structure (B1) is taken as $a(\text{Å}) = a_0(\text{Å})/\sqrt{2}$ where $a(\text{Å})$ is the lattice constant.

	InP		**$Y_{0.25}In_{0.75}P$**		**$Y_{0.5}In_{0.5}P$**		**$Y_{0.75}In_{0.25}P$**		**YP**	
	B1	**B3**	**B1**	**B3**	**B1**	**B3**	**B1**	**B3**	**B1**	**B3**
a (Å)	3.92, 3.93[a] 3.92[c]	5.96, 5.97[a], 5.98[b], 5.968[c], 5.869[d]	3.95	6.07	3.99	6.17	4.00	6.24	4.01, 4.02[g], 4.01[h]	6.29
(c/a)	$\sqrt{2}$	1	$2\sqrt{2}$	1	$2\sqrt{2}$	1	$2\sqrt{2}$	1	$\sqrt{2}$	1
V_0 (Å^3)	42.57*, 42.66[a], 42.57[c]	53.04, 53.15[c]	43.70	56.04	45.09	58.67	45.33	60.73	45.62	62.26
B (GPa)	73.41, 78.48[a], 73.2[c]	59.60, 59.3[c]	73.73	54.84	74.71	53.10	78.29	53.21	84.24	56.72
E_{Coh}(eV/ unit cell)	-4.44, -5.61[c]	-4.92, -6.09[c]	-5.95	-6.01	-7.56	-7.25	7.28	-8.57	-11.08, -11.02[g]	-9.99

[a]Ref.[41], [b]Ref.[42], [c]Ref.[20], [d]Ref.[43],[e]Ref.[44],[f]Ref.[45], [g]Ref.[29], [h]Ref.[38].

To examine the phase change between ZB and NaCl phases under the influence of pressure of $Y_xIn_{1-x}P$ alloys, we have used the enthalpy free energy given by: H = U+PV where U is the internal energy, P is the pressure and V is the volume. It is evident from the theory of thermodynamics that the transition phase P_T is determined where the enthalpy free energy of both structures is the same. The enthalpy-pressure figure of $Y_xIn_{1-x}P$ alloys are illustrated in Fig.2. The calculated P_T are listed in the Table 2 and shown that the pressure transition of $Y_xIn_{1-x}P$ alloys from B3 to B1 occurs only for $x = 0$ and $x = 0.25$. For InP ($x = 0$) P_T is predict at 9.23 GPa which agree with other experiment values [46],[47] and other theoretical calculations [48-50]. For $x = 0.25$, the P_T is observed at 0.96 GPa, for our knowledge, no reported data for this transition pressure. For the $x = 0.5$, $x = 0.75$ and $x = 1.0$, we have no possible phase transition between B3 and B1. The volume reduction across the B3 to B1 transition of about 18% and 21.7% of InP and $Y_{0.25}In_{0.75}P$ respectively.

Table2. Transition pressures of $Y_xIn_{1-x}P$ alloys and their volumes change.

	InP Experiment Values		**Other calculations**	**$Y_{0.25}In_{0.75}P$**
P_T(GPa)	9.23	9.8[a], 10.8[b]	10[c,d], 8.9[f]	0.96
V_{B3}(Å^3)	47.08		48.87[e]	55.10
V_{B1}(Å^3)	38.51		39.87[e]	43.14
ΔV(Å^3)	8.57		9[e]	11.96

[a]Ref.[46], [b]Ref.[47], [c]Ref.[48], [d]Ref.[49], [e]Ref.[50],[f]Ref.[41].

To analyse the alloying stability of structures, we have calculated the cohesive energy as a function of Y concentration in both rock salt and zinc blende like structures, which for the binaries, the cohesive energy was obtained by subtracting their total energy of $Y_xIn_{1-x}P$ alloys at their equilibrium lattice constants from the energy of the relevant isolated (Y, In and P) atoms. For the ternary, the cohesive energy was calculated by subtracting from their total energy of binaries, each one multiplied by its fraction. The results of cohesive energy are plotted in Figure.3.

From Figure 3, we conclude that for the concentration of Y concentration less than 30% the most stable phase is ZB-like structure and rock salt like structure becomes stable beyond 30%.

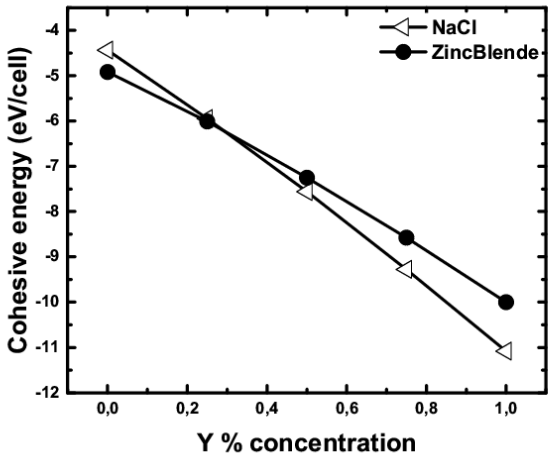


Figure 3. Cohesive energy versus Y concentration for $Y_xIn_{1-x}P$ in rock-salt and zinc blende-like structures

To confirm the structural stability, we have used Cubic code [51], to obtain the elastic constants of the $Y_xIn_{1-x}P$ alloys, based on the second-order derivative of the polynomial fit of energy versus strains to the equilibrium unit cell. For a cubic system, the case of zinc blende-like structure, there are three independent elastic constants $C_{11}, C_{12}$and C_{44}, where C_{11} and C_{12} describe the crystal response in tension, while C_{44} describes the crystal response to shear strain. The calculated of independent elastic constants of $Y_xIn_{1-x}P$ alloys in the stable configurations are summarized in Table 3.

The mechanical stability of $Y_xIn_{1-x}P$ compounds can be checked by the following criteria for cubic crystals [52]:

$$C_{11} - C_{12} > 0,\ C_{11} > 0,\ C_{44} > 0,\ C_{11} + 2C_{12} > 0 \text{ and } C_{12} < B < C_{11} \quad (1)$$

For the tetragonal system the case of the rock salt-like structure, there are six independent elastic constants $C_{11}C_{12}$, C_{13}, C_{33}, C_{44} and C_{66}. The stability conditions for this tetragonal system are [2]:

$$C_{33} > 0,\ C_{44} > 0,\ C_{66} > 0,\ C_{11} > |C_{12}|,\ C_{11} + C_{12} > 0 \text{ and } C_{11} + C_{33} - C_{13} > 0.$$

As shown in Table 3, our calculated values of elastic constants fulfil all mentioned criteria, which indicate that $Y_xIn_{1-x}P$ compounds are mechanically stable in both NaCl and ZB-like structures.

Table3. Elastic constants $Y_xIn_{1-x}P$ alloys in their stable configurations.

Stable configurations	InP	$Y_{0.25}In_{0.75}P$	$Y_{0.5}In_{0.5}P$	$Y_{0.75}In_{0.25}P$	YP
	Zinc Blende-like structure		NaCl-like structure		
C_{11}(GPa)	88.38 101.1[a] 102.2[b],109.5[c]	73.71	128.50	138.30	204.06, 199[d]
C_{12}(GPa)	47.83 56.1[a], 57.6[b],55.7[c]	46.71	51.52	48.68	28.42, 28[d]
C_{44}(GPa)	60.80 45.6[a], 46.0[b], 52.6[c]	50.81	21.00	34.09	49.17, 47[d]
C_{13}(GPa)			29.56	25.04	
C_{33}(GPa)			147.42	148.66	
C_{66}(GPa)			66.47	69.58	

[a]Ref.[53], [b]Ref.[54], [c]Ref.[55], [d]Ref.[56].

3. 2. Electronic properties

The electronic properties of $Y_xIn_{1-x}P$ alloys for different Y concentrations were calculated for the corresponding stable configurations. In the previous section, we have found that for the concentration less than 30% (InP and $Y_{0.25}In_{0.75}P$) the stable configuration is Zinc blende-like structure. While the rock-salt-like structure for the other concentrations. The calculated band structure along with high symmetry directions and related total and partial density of state (TDOS and PDOS) of $Y_xIn_{1-x}P$ alloys are shown in Fig. 4, in the correspondent stable configurations. The Fermi level is set at 0 eV for the concentration less than 30% ($x = 0$ and $x = 0.25$) the stable configuration is Zinc blende-like structure. In pure InP the band structure is showed in Fig.4a, which the maximum of the valence band and the minimum of the conduction band situated at Γ point, therefore InP exhibits a direct transition with an energy gap of about 1.43 eV, which confirms the semiconductor behavior. This value is in good agreement with the experimental value at T=0 K, Eg= 1.423 eV [57] and better than predicted other theoretical values 1.33 eV [41] and 1.374 eV [58]. Employing the mBJ potential yields a better estimation of the band gaps of semiconductors over the LDA and GGA potentials [35]. Total and partial density of state (TDOS and PDOS) of InP illustrated in Fig4a. The upper region of Band Valence (BV) is sharped in two peaks, the first peak is originated from P(p) and In(S). The second peak near the Fermi level is formed by P(p) and In(p) orbitals. The bottom region of the conduction band (BC) is characterized mainly by the p-orbital of phosphide (P) atom and In(s). We noticed the week contribution of In(d) state in both valence and conduction regions. These results of InP appear similar to other theoretical works [41], [35]. For the $Y_{0.25}In_{0.75}P$ alloy, when pure InP is doped by 25% y concentration, the band structure depicted in Fig.4b keeps the Zinc Blende configuration and shows an enlarged direct

band gap by 34% ($E_g = 2.17\,eV$). The analysis of TDOS and PDOS show that two peaks constitute the top of valence band region. The upper one is dominated by strong hybridization between P(p)-Y(d) and a visible contribution of In(p) bands and that DOS is nonzero at E_F.

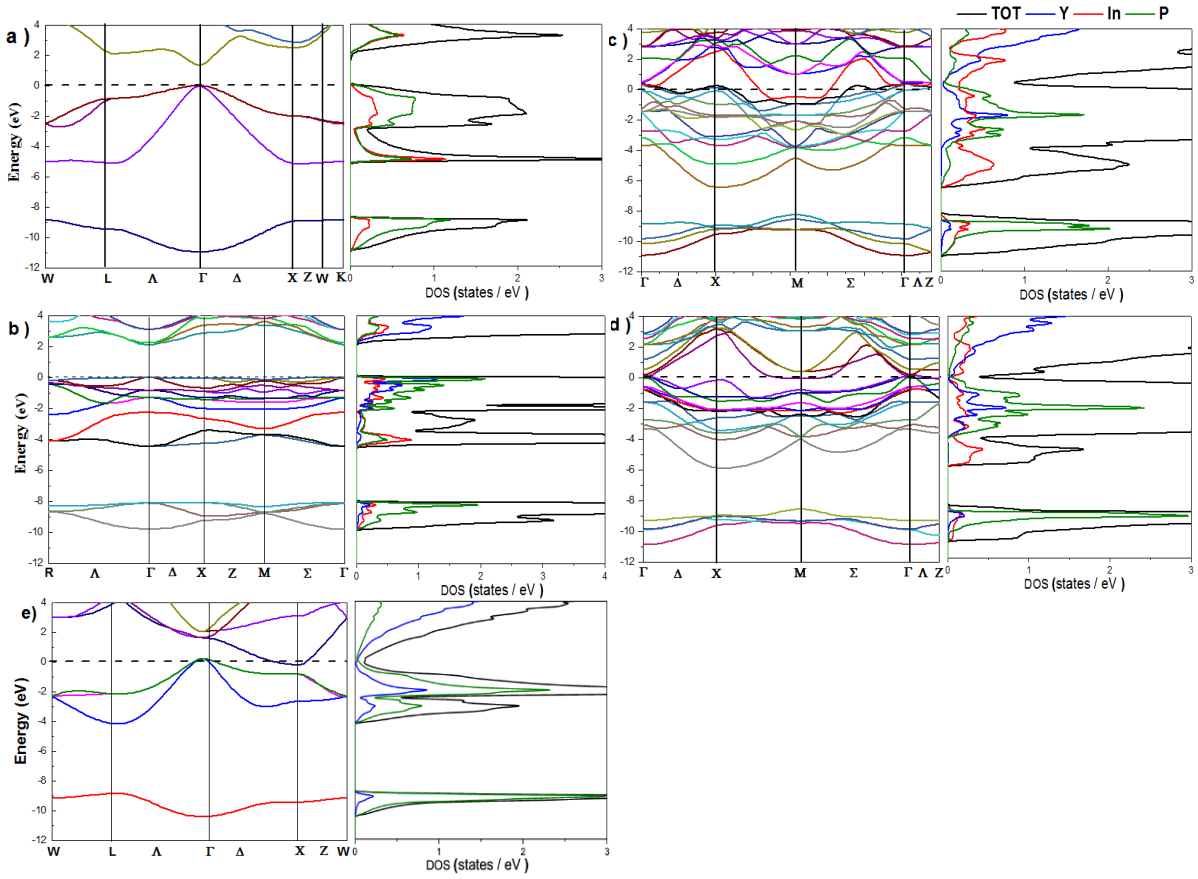


Figure 4. Band structures and density of states (Total and Partial) calculated for $Y_xIn_{1-x}P$: (a) InP in the Zinc-blende structure, (b) $Y_{0.25}In_{0.75}P$ in the Zinc blende-like structure, (c) $Y_{0.5}In_{0.5}P$ in the rock-Salt-like structure, (d) $Y_{0.75}In_{0.25}P$ in the rock salt--like structure and (e) YP in the rock-salt structure. Zero energy level show the Fermi energy

The CB is formed mainly by In(s), P(p) and Y(d) derived states broaden further and shift up in energy. We noted that In(d) remained small and insignificant as in the pure InP. Figs (4c, 4d, 4e) show that $Y_xIn_{1-x}P$ alloys in the cases (50%, 75%, and 100% of Y) all in the rock-salt-like structure, which is the more stable configuration in the range $0.30 \leq x \leq 1$. From the Figs (4c, 4d, 4e) the Fermi level crosses the valence with major contribution is made from P(p). The lower one is formed mainly by In(s) and P(p) states. However, these compounds exhibit metallic behavior. For YP case 100% of Y, our results concord with previous theoretical works [21]. From the PDOS showed in Fig (4e), it seems that the BV is dominated by hybridization between P(p) and Y(d) orbitals with a large contribution from P(p) state. The opposite trend appears in the BC. The related PDOS of 50% and 75% of Y present a similar contribution of atom orbitals. The BV is split into two peaks, the upper peak originates mainly from P(p) and

Y(d). The lower peak is mainly attributed to In(s) while the BC is originated from In(p) and Y(d).

To see the influence of 4d state of Y atom, we plot together with the PDOS of pure InP and doped InP in the case 25% of Y and illustrated in Fig.5. We observed that all peaks are shifted upward in energy in both valence and conduction bands from InP to $Y_{0.25}In_{0.75}P$ alloy affected by the incorporation of Y atom in the InP matrix. Also, a large contribution of 4d(Y) near the top of Fermi level and lower of conduction band is there. We can clearly see that the gap increases with increasing of Y concentration ($x = 25\%$), additional opening of the gap is due to push up of 3p (P) about 0.7 eV in the lower BC. To our knowledge, these $Y_xIn_{1-x}P$ alloys (x= 25%, 50%, and 75% of Y) were not investigated previously, however, no competitive data to compare the present results.

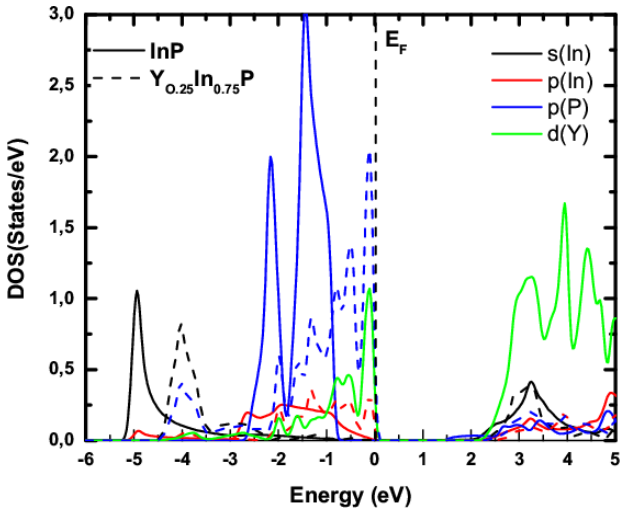


Figure 5. Partial density of states (PDOS) of InP and $Y_{0.25}In_{0.75}P$ in the same scale

3. 3. Enthalpy of mixing and alloy phase diagram

To confirm the corresponding transition concentration value founded in the structural property section, we have investigated the enthalpy of mixing and alloy phase diagram based on the regular-solution model [59]. The thermodynamic stability is estimated at zero temperature and normal pressure, results from comparing calculated total energies of the ternaries $Y_xIn_{1-x}P$ in the different concentrations with the binaries parents with have different ground state phases ZB-like and NaCl respectively. Hence, the solid solution $Y_xIn_{1-x}P$ would proceed into two-phase mixture. For ZB and NaCl phases, we assume that the enthalpy of mixing can be obtained from the calculated total energies by the expression:

$$\Delta H_m = E^{Tot}[Y_x In_{1-x} P] - [xE^{Tot}(YP) + (1-x)E^{Tot}(InP)] \quad (2)$$

Where $E^{Tot}[Y_xIn_{1-x}P]$, $E^{Tot}(YP)$ and $E^{Tot}(InP)$ are the total energies of ternaries, YP and InP respectively. The difference between the enthalpy and the total energy is insignificant for a solid or a liquid [60]. The alternative form of the enthalpy of mixing is expressed as:

$$\Delta H_m = \Omega . x . (1 - x) \tag{3}$$

Where, Ω is the interaction parameter which depends on the material and x correspondent to the concentration. In addition, the enthalpy of mixing phases ΔS_m given by the following form:

$$\Delta S_m = -RT[xlnx + (1 - x)\ln (1 - x)] \tag{4}$$

Where, R stands for gas constant. The contribution of enthalpy comes in part from disorder configuration and in other part from the lattice vibration that is neglected in this study (for semiconductor alloys).

The Gibbs free energy of mixing phases $\Delta G_m$is expressed as:

$$\Delta G_m = \Delta H_m - T\Delta S_m \tag{5}$$

Where ΔH_m and ΔS_m are the enthalpy and entropy of mixing defined previously, and T the absolute temperature.

The obtained results of enthalpy of mixing are shown in Fig. 6. Where, we have calculated firstly, the interaction parameter Ω(x) values (per cation-anion pair) from the linear fit named x-dependent interaction parameter and average value named x-independent parameter respectively. The linear fit gives $\Omega(x) = 1.177x - 0.015$ eV/pair and $\Omega(x) = 1.177x - 0.015$ eV/pair, the average value of interaction parameter in the range $0 \leq x \leq 1$ are $0.57\ eV$/pair and $0.47\ eV$/pairfor ZB-like and NaCl respectively. Secondly, the enthalpy of mixing values extracted from first principle calculations of ZB and NaCl were fitted to the polynomial function and according to the interaction x-dependent or independent parameter form. Figure 6 shows that the enthalpy of mixing is symmetric using the average values of the x-independent for both rock-salt and zinc-blende structures. While, ΔH_m is asymmetric using the x-dependent interaction parameter leading to a slight deviation for ZB on the lower-x and NaCl being higher-x with the crossing point near 0.30. This result indicates that the ZB phase is more stable than the NaCl phase in the concentration range below 0.30. However, we

observed the opposite behavior in the range $0.30 \leq x \leq 1$. Hence, the results confirm the corresponding transition concentration value founded in the structural property section. The mixing enthalpy of $Y_xIn_{1-x}P$ alloys is positive for both ZB and NaCl phase indicating that the system tends to segregate to their constituents at normal growth temperatures [30]. The similar trend is observed in the $Sc_xGa_{1-x}P$,$Sc_xY_{1-x}P$ and $Sc_xIn_{1-x}P$ systems [20],[21],[30].

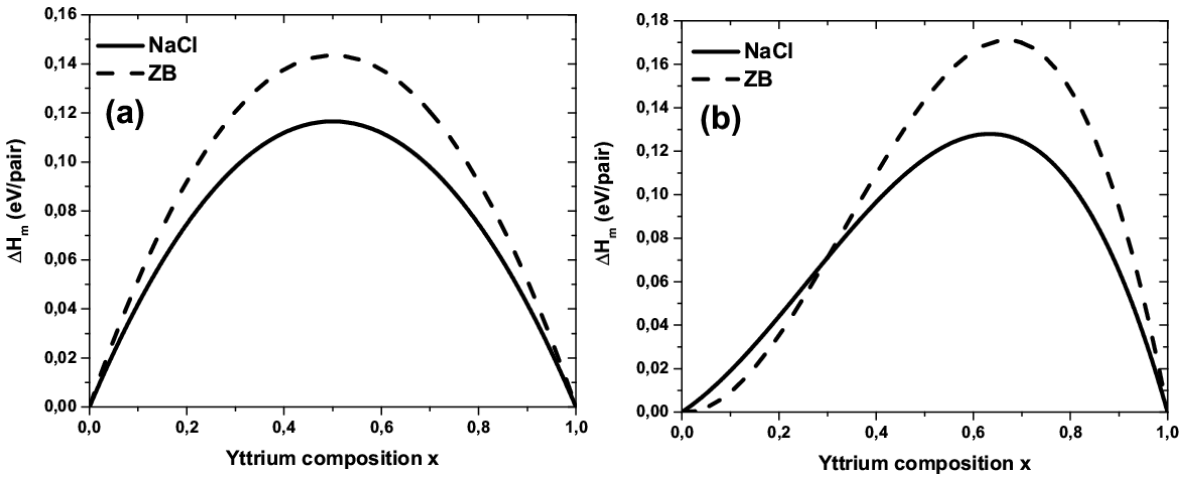


Figure 6. Mixing enthalpy ΔH_m per cation-anion pair as e function of Yttrium concentration for the $Y_xIn_{1-x}P$ a) x-independent interaction parameter b) x-dependent interaction parameter

Figure 7 shows the T-x phase diagram of $Y_xIn_{1-x}P$ alloys and their critical alloy formation temperature Tc that marking the solubility limits below which phase separation will occur. Tc is 3441K in absence of vibrational contribution. According to the binodal and spinodal curves, the T-x phase diagram shows the stable, metastable and unstable mixing regions of the alloys. The binodal (spinodal) curve corresponds to the first (second) derivative of the free energy of mixing ΔG_m are set to zero at different concentrations. The critical alloy formation temperature Tc occurs at a point where the bimodal and spinodal curves touch. We remember that the spinodal curve in the phase diagram marks the equilibrium solubility limit [60]. Our results indicate that the$Y_xIn_{1-x}P$ alloys are stable at high temperature.

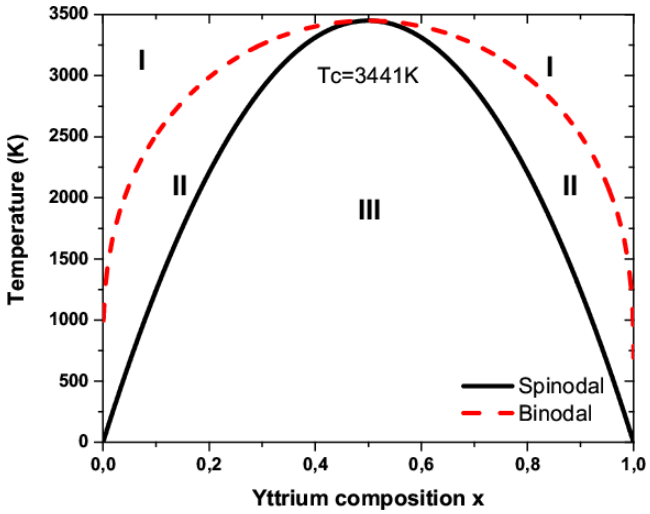


Figure 7. Mixing enthalpy ΔH_m per cation-anion pair as e function of Yttrium concentration for the $Y_xIn_{1-x}P$ in the case x-dependent interaction parameter. I, II and III designed the Stable, metastable and unstable regions respectively

3. 4. Optical properties

The optical properties of solids have been proven to be a powerful mean for understanding the atomic and electronic structure of semiconducting materials. We present now the analysis of the optical spectra for obtaining further insight into the electronic structure of $Y_xIn_{1-x}P$ alloys in the case ($x = 0$ and $x = 25\%$). The imaginary part of the optical dielectric function $\varepsilon_2(\omega)$, is of fundamental importance and can be used to explain features of linear response of the system to electromagnetic radiation [61].

$$\varepsilon_2(\omega) = \frac{4\pi^2 e^2}{m^2\omega^2}\sum_{ij}\int_{BZ}\left|\langle i|M|j\rangle\right|^2 f_i(1-f_i)\delta\left(E_f(k)-E_i(k)-\omega\right)d^3k \qquad (6)$$

where M is the dipole matrix, i and j are the initial and final states respectively. The Fermi distribution function for the i^{th} state is represented as f_i the electron energy in the ith state. The real part of optical dielectric function,$\varepsilon_1(\omega)$, is derived from the corresponding imaginary part of dielectric function,$\varepsilon_2(\omega)$ using the Kramer-Kroning relationship.

Optical properties such as refractive index $n(\omega)$, extinction coefficient $k(\omega)$, absorption coefficient $\alpha(\omega)$, optical conductivity $\sigma(\omega)$, and reflectivity $R(\omega)$ can be derived directly from the calculated spectra of $\varepsilon_1(\omega)$ and $\varepsilon_2(\omega)$. The crystal structure of $Y_xIn_{1-x}P$ alloys is cubic and its optical properties are isotropic. Hence, for our analysis, only one of the dielectric tensor components $\varepsilon_{xx}(=\varepsilon_{yy}=\varepsilon_{zz})$ is sufficient for calculating the other optical properties. The polarizability of the crystal is related to imaginary part of the optical dielectric function $\varepsilon_2(\omega)$, and provides information about the light absorption in materials. The material is said to be

transparent until the absorption begins at which $\varepsilon_2(\omega)$ will become non-zero [61]. The calculated imaginary part of the dielectric function of InP and $Y_{0.25}In_{0.75}P$ is shown in Fig.8. The main feature of $\varepsilon_2(\omega)$ for $Y_{0.25}In_{0.75}P$ shows two peaks with higher intensity around 3 eV and 4.6 eV. The optical spectra are results of the inter-band transition of electrons from VB to CB. The interband optical transition analysis show that the peak around 3 eV (4.6 eV) correspond mainly to the interband optical transitions arising from VB originating from P-2py and P-2px located in the VBM to Y-4dxy and Y-4dx^2y^2 states in the CB.

For InP, the feature in $\varepsilon_1(\omega)$ shows also two peaks at 2.9 eV and 4.4 eV (3 eV and 4.5 eV for real data), after that $\varepsilon_1(\omega)$ becomes negative above 4.7 eV. The frequency at which the zero crossing of $\varepsilon_1(\omega)$ becomes negative. The frequency at which the zero crossing of $\varepsilon_1(\omega)$ occurs corresponds to the location of plasma frequency, and above which the material shows a dielectric behavior. For $Y_xIn_{1-x}P$ alloys in the case ($x = 25\%$), $\varepsilon_1(\omega)$ crosses zero at $E = 4.1eV$. The extinction coefficient, $k(\omega)$ shows the two peaks at same energy position as $\varepsilon_2(\omega)$. The transition from P-2py state to In-1s state may drive to the peak at this energy range, and the first peak is attributed to $L^v \rightarrow L^c$ by electronic band structure [62]. The spectra of refractive index $n(\omega)$ have similar frequency dependent features like $\varepsilon_1(\omega)$ spectra. We note that the intensity of the first peak is much higher than the experimental curve of about one order of magnitude, but this is a general feature of all theoretical spectra [63].

Fig.8 shows further the effect of the broadening parameter ($\eta = 0$ and $\eta = 0.1$) on the α spectrum. The experimental spectrum and the TB-mBj spectrum of $\eta = 0$ are consistent with those shown in Fig.8. This effect also have been shown by [63] using HSE06 calculation and this is artifact caused by smoothening of the calculated $\varepsilon_1(\omega)$spectrum.

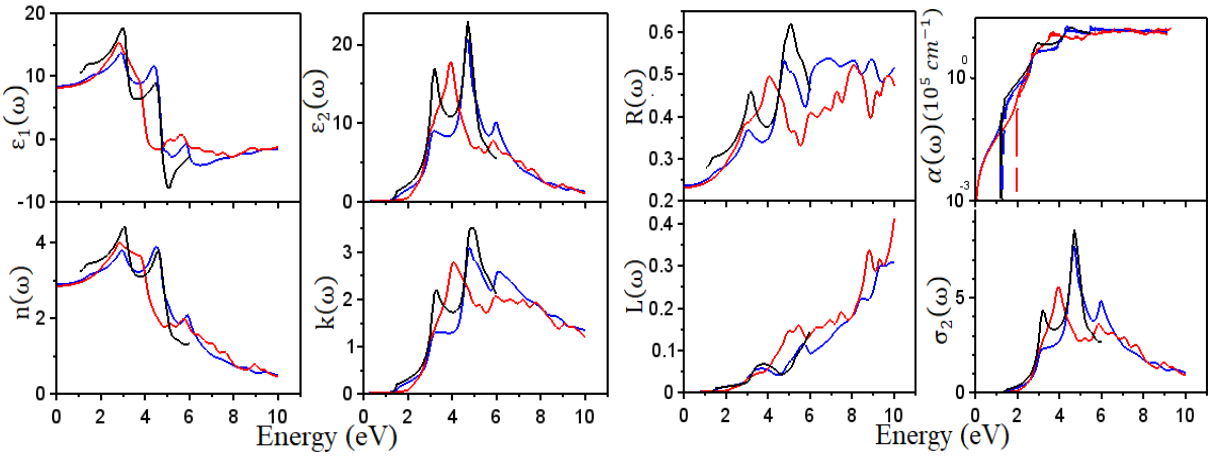


Figure 8. The calculated optical spectra for InP (blue) and $Y_{0.25}In_{0.75}P$ (red). The black curves are for experimental data [69], [70]

The absorption spectra, ($\alpha(\omega)$) has a sharp two peaks at 2.9 eV and 4.4 eV and this may come from the inter-band optical transitions from P-2py to In-1s states. The absorption spectra is reasonably high (>$10^5 cm^{-1}$) for for$Y_xIn_{1-x}P$ alloys in the case ($x = 0$ and $x = 25\%$). In addition to an increase of gap of $Y_{25}In_{0.75}P$. The reflectivity shows less than 30% around the energy value of 2 eV. The $\sigma_2(\omega)$ spectrum is having same spectral distribution as the $\varepsilon_2(\omega)$ spectra due to the obsorptive nature of the $\sigma_2(\omega)$. The studies of electron energy loss spectrum (EELS), $L(\omega)$, is important for the description of microscopic and macroscopic properties of solids, and represents energy loss characteristics (plasmon oscillation). The highest peak in the L(w) spectrum is considered as the Plasmon peak and that is at 14.7 eV (not shown the figure) in L(w) spectra corresponds to that $\varepsilon_1(\omega) = 0$, and this gives the plasma resonance. The plasma resonance was found the same for $Y_xIn_{1-x}P$ alloys in the case ($x = 0$ and $x = 25\%$).

3. 5. Photovoltaic properties

When a solar cell is illuminated, only the photons having energy higher than the band gap energy (E_g) of the semiconductor are absorbed and create electron hole-pairs [64]. The photo-generation of electron–hole pairs in the semiconductor depends on the incident photon flux and the absorption coefficient ($\alpha(\omega)$) of incident light in the semiconductor [65]. To evaluate the photovoltaic performance of InP and $Y_{0.25}In_{0.75}P$ as an ideal solar cell, its PV conversion efficiency is simulated in this work. This is done by using the spectroscopic limited maximum efficiency (SLME) method [65]. The maximum short-circuit current density obtained from an absorbent material can be estimated by:

$$J_{sc} = e\int_{Eg}^{+\infty} I_{sun}(E)dE \tag{7}$$

However, by taking into account the frequency dependence of absorption coefficient $\alpha(E)$ and the thickness L equation **(7)** becomes:

$$J_{sc} = e\int_{Eg}^{+\infty}(1 - e^{2\alpha(E)L})I_{sun}(E)dE \tag{8}$$

where, E_g stands for the energy gapband.

In semiconductors $E_g$varies with temperature, and to calculate the short-circuit current density J_{sc}, we need to evaluate the band gap $E_g(T)$ for InP and $Y_{0.25}In_{0.75}P$ at any temperature T. As first approximation, Varshni expression [64] is used for that purpose:

$$E_g(T) = E_g(0) + \frac{\alpha T^2}{T+\beta} \quad (9)$$

The parameters $\alpha = 4.9\ 10^{-4}\ eVK^{-1}$ and $\beta = 93\ K$ are used for both compounds (InP and $Y_{0.25}In_{0.75}P$).

After calculating J_{sc}, the total current density harvested in a solar cell is :

$$J = J_{sc} - J_D \quad (10)$$

Where J_D is the recombination current density which is calculated by:

$$J_D = J_0\ (exp\left(\frac{qV}{kT}\right) - 1) \quad (11)$$

where V is the electrical potential over the absorber layer, q is the elementary charge, k is the Boltzmann's constant and J_0 is reverse saturation current density. The J_0 is an important diode parameter which controls the change in performance parameters with temperature and its effect was investigated in [67]. A good approximation of J_0 is given by:

$$J_0 = C.T^3.exp\left(-\frac{E_g}{k.T}\right) \quad (12)$$

where $C = 17.90\ cm^{-2}K^3$ is a constant.

Table 4. Compared solar cell parameters performance for a thickness of $L = 1\ \mu m$.

Materials	$\boldsymbol{\eta}$ (%)	**Jsc** (A/m^2)	$\boldsymbol{V_{oc}(V)}$	$\boldsymbol{FF}$(%)
InP (real data)	28.35	34.92	0.93	88
InP (simulated data)	24.90 (24.2*)	30.79 (31.15*)	0.92 (0.94*)	88 (83*)
$\mathbf{Y_{0.25}In_{0.75}P}$	18.34	12.36	1.62	92

*experimental reported data [66].

In our SLME model we have neglected the series resistance R_s in eq.11 and we assumed here only the flat front surface with a perfectly reflective mirror on the back surface. Three parameters are important quantify the efficiency of a solar cell: J_{sc}, the open-circuit voltageV_{oc} and the Fill Factor FF. The open-circuit voltage V_{oc} corresponds to the voltage where $J = 0$, and is given by:

$$V_{oc} = \frac{kT}{q} \ln\left[\frac{J_{sc}}{J_0} + 1\right] \quad (13)$$

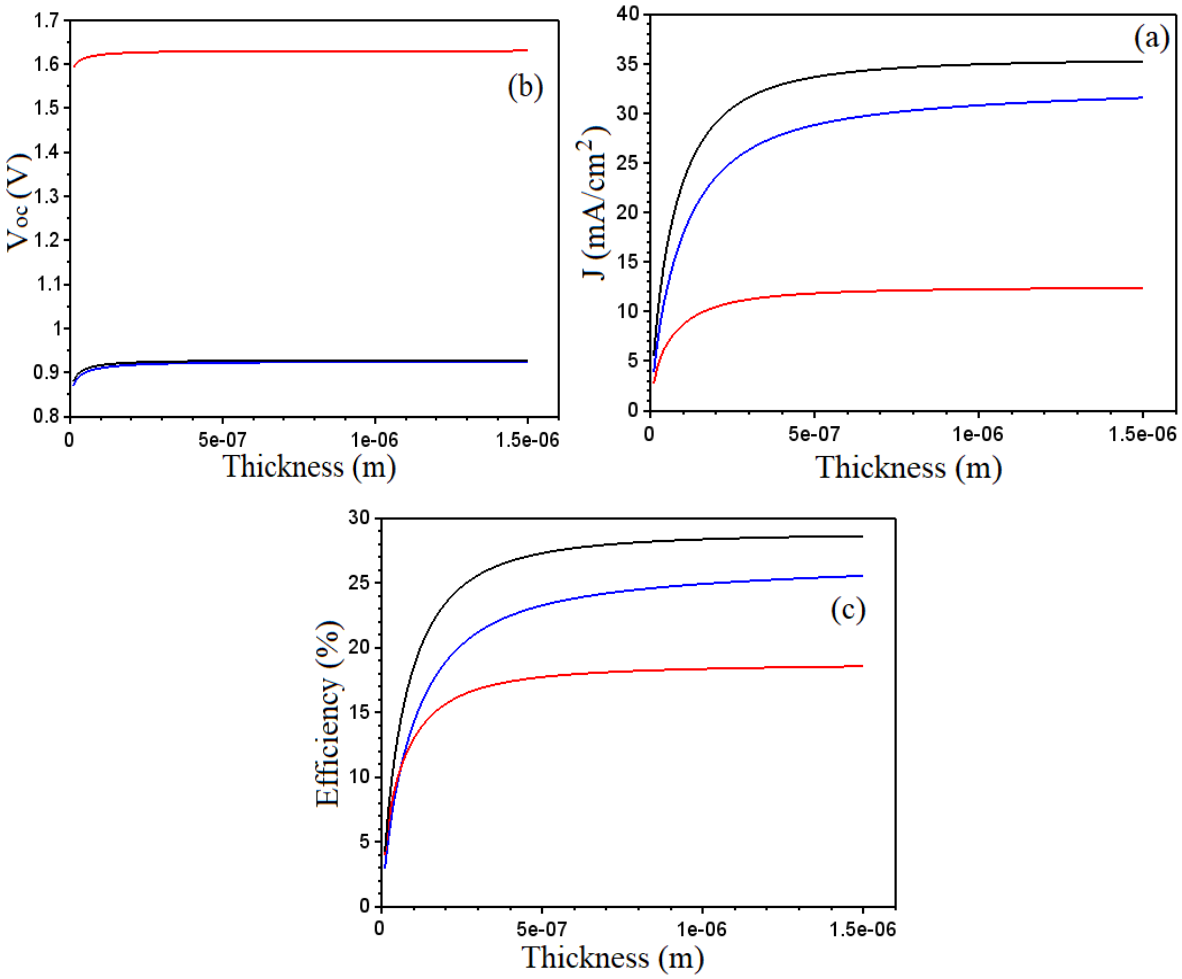


Figure 9. Simulated J_{sc}, V_{oc} and η for InP (blue) and $Y_{0.25}In_{0.75}P$ (red). The black curves are obtained from experimental data of $\alpha(\omega)$

And the fill factor can be approximated by [68]:

$$FF = \frac{v_{oc} - ln(v_{oc}+0.72)}{v_{oc}+1} \tag{14}$$

where $v_{oc} = \frac{q}{kT} V_{oc}$ is defined as a normalized V_{oc}, and finally the efficiency η is estimated via:

$$\eta(\%) = J_{sc}.FF.V_{oc}/0.1(W/cm^2) \tag{15}$$

The calculated J_{sc}, V_{oc} and η for InP and $Y_{0.25}In_{0.75}P$ are showed in Fig.9. Our results for J_{sc}, V_{oc} and η in function of thickness L are resumed in Table 4. A thickness of $L = 1\mu m$ is enough to confirmed the experimental data as indicated in Table 4. In Table 4, the real data are the measured data [69],[70] of absorption coefficient $\alpha(E)$ which we have used to calculate J_{sc}.

For the $Y_{0.25}In_{0.75}P$ alloy an efficiency of 18% can be achieved as shown in Fig.9 and Table 4. The matching of lattice constant (a mismatch < 4%) of InP and $Y_{0.25}In_{0.75}P$ lead to negligible interface defects. The $Y_{0.25}In_{0.75}P$ alloy has a wider bandgap than InP and would allow most solar photons to pass through. These issues made $Y_{0.25}In_{0.75}P$ suitable for tandem solar cells ($Y_{0.25}In_{0.75}P$/AnP) and quantum wells ($Y_{0.25}In_{0.75}P$/AnP/ $Y_{0.25}In_{0.75}P$) applications.

4. Conclusion

In summary, the structural, optoelectronic and photovoltaic properties of pure and doped InP were investigated using the DFT with GGA for potential exchange-correlation. The mBJ-GGA potential approximation was also used for calculating the optoelectronic properties of these materials. The SLME was used to calculate the efficiency η of the pure and doped InP solar flat cells. Our results can be summarized as follows:

i) A reasonable lattice mismatch between InP and YP allow to combination as $Y_xIn_{1-x}P$ alloys, therefore, parameter lattice increases accompanied by an increase of the bulk modulus (B) with respect to the incorporation of Y atoms, opposite trend is observed of the bulk modulus confirming that $Y_xIn_{1-x}P$ alloys are more rigid in rock-salt structure compared to zinc-blende structure.

ii) The results of cohesive energies and elastic constants calculation imply that these compounds exhibits energetic and mechanical stabilities and suggest that they can be prepared and stabilized experimentally.

iii) We also report the pressure transition of $Y_xIn_{1-x}P$ alloys from B3 to B1 occurs only for x =0 and x = 0.25. For InP (x= 0) P_T is predict at 9.23 GPa, while is observed at 0.96 GPa, for x=0.25.

iv) The substitution of In by Y atom is found to be able to enlarged the direct bandgap from 1.43 eV to 2.17 eV of about 34% and confirms the semiconductor behavior which is caused by push up of 3p (P) about 0.7 eV in the lower BC.

v) The mixing enthalpy of $Y_xIn_{1-x}P$ alloys is positive for both ZB and NaCl phase indicating that the system has tendency to segregate to their constituents at normal growth temperatures with a critical temperature of 3441K.

vi) The absorption spectra is reasonably high (>$10^5 cm^{-1}$) for for$Y_xIn_{1-x}P$ alloys in the case (x=0 and x=25%). An efficiency solar cell of 18% can be achieved. Also, a thickness of $L = 1\mu m$ is enough to confirm the experimental data. These results predict that zinc-blende $Y_xIn_{1-x}P$ alloys are promising candidate for optoelectronic and photovoltaic devices. Regarding tothe matching of lattice parameters (a mismatch < 4%) of InP and $Y_{0.25}In_{0.75}P$

and the bandgap energy difference made $Y_{0.25}In_{0.75}P$ suitable for Tandem solar cells ($Y_{0.25}In_{0.75}P$/InP) and quantum well ($Y_{0.25}In_{0.75}P$/InP/$Y_{0.25}In_{0.75}P$) applications.In the absence of experimental works, our results can be useful for further studies.

References

[1] J.Y. Tsao, S. Chowdhury, M. A. Hollis, D. Jena, N. M. Johnson., K. A. Jones, K and C. L. Chua. Adv. Electron. Mater. (2018) *4*(1), 1600501

[2] S. Adachi, *Properties of Semiconductor Alloys: Group-IV, III-V and II-VI Semiconductors*, Wiley Series in Materials for Electronic and Optoelectronic Applications, John Wiley and Sons Ltd., (2009)

[3] M.R. Krames, O. B, Shchekin, R. Mueller-Mach, G. O. Mueller, L. Zhou, G. Harbers, G and M. G. Craford. J. Disp. Technol. (2007) 3, 160

[4] T. Kim, B. Wang, C.Wang, D. A. Kohen, J. W. Hwang, J. C. Shin, J. C and J. Michel. *Journal of Vacuum Science & Technology A: Vacuum, Surfaces, and Films*. (2017) *35*(3), 031507

[5] A.E. Henkes, Y. Vasquez and R.E. Schaak. J. Am. Chem. Soc. 2007, *129*(7), 1896

[6] T. M. Christian, D. A. Beaton, K. Mukherjee, K. Alberi, E. A. Fitzgerald, and A. Mascarenhas, J. Appl. Phys. (2013) 114, 074505

[7] M. Rezek , K. Senay. J. ALLOY. COMPD. (2009) 478 531

[8] M. Rezek , K. Senay. J. ALLOY. COMPD. (2009) 485 687

[9] J. Chamings, S. Ahmed, and S. J. Sweeney, V. A. Odnoblyudov and C. W. Tu. Appl. Phys. Lett. (2008) 92, 021101

[10] A. González-García, W. López-Pérez, W, R. Palacio-Mozo and R. González-Hernández, *Thermodynamic properties of In1− xBxPsemiconducting alloys: A first-principles study*, Comput. Condens. Matter. (2014) 91, 279.

[11] M. Gandouzi, F. Hedhili, and N. Rekik. Comput. Mater. Sci. (2018) 149, 307-315.

[12] Yu. Zhang, Ya. Zhang, C. Wang, and Y. Zeng, J. Appl. Phys. (2013) 114, 243710

[13] C.-G. Maa, V. Krasnenko, and M. G. Brik, Solid State Commun. (2015) 205, 55

[14] H. B. Russell, A. N. Andriotis, M. Menon, J. B. Jasinski, A. Martinez-Garcia, and M. K. Sunkara. Sci. Rep. (2016) 6(1), 1

[15] S. Lakel, F. Okbi, and H. Meradji. Optik, (2016) 127(8), 3755

[16] A. Abdollahi, M. M Golzan, and K. Aghayar, K. J. Mater. Sci. (2016) 51(15), 7343-7354

[17] A.R. Degheidy, E. B. Elkenany, and O. A. Alfrnwani. Comput. Condens. Matter. (2018) 16, e00300

[18] E. Okbi, S. Lakel, S. Benramache, S, and K. Almi. Semicond. (2020) 54(1), 58-66

[19] M.Othman, E. R. Kasap, and N. Korozlu. Journal of Alloys and Compounds. (2010) 496(1-2), 226-233

[20] W. López-Pérez, N. Simon-Olivera, J. Molina-Coronell, A. González-García, and R. González-Hernández. J. ALLOY. COMPD. (2013) 574, 124-130

[21] W. López-Pérez, P. Castro-Diago, L. Ramírez-Montes, A. González-García, and R. González-Hernández. Philos Mag. (2016) 96(5), 498-510

[22] Moram, M. A., & Zhang, S. J. Mater. Chem. A. (2014) 2(17), 6042

[23] Y. Cherchab, B. Amrani, N. Sekkal, M. Ghezali and K. Talbi, Physica E (2008) 40, 606.

[24] M. G. Moreno-Armenta, L. Mancera, and N. Takeuchi. Phys. Status. solidi (b). (2003) *238*(1), 127

[25] S. Mokkapati, and C. Jagadish. Mat. Today, (2009) 12(4), 22

[26] M.J.W. Rodwell, M. Urteaga,, Y. Betser, T. Mathew, P. Krishnan, D. Scott, and R. P. Smith. Int. J. High Speed Electron. Syst. (2001) 11, 159

[27] C.S. Menoni, I.L. Spain, Phys. Rev. B. (1987) 35, 7520

[28] I. Vurgaftman, J.A. Meyer, and L. A. Ram-Mohan. J. Appl. Phys. (2001) 89(11), 5815.

[29] B. Amrani, F. El Hadj, Comput. Mater. Sci. (2007) 39, 563

[30] W. Celin-Mancera, W. López-Pérez, Á. González-García, L. Ramírez-Montes,, and R. González-Hernández. Comput. Condens. Matter. (2016) 8, 14-21

[31] M. Othman, E. R. G. Ü. N. .Kasap, and N. Korozlu, N. Physica B: Condensed Matter. (2010) 405(10), 2357

[32] P. Blaha, K. Schwarz, G.K.H. Madsen, D. Kvasnicka, J. Luitz, WIEN2k*, An Augmented Plane Wave Plus Local Orbitals Program for Calculating Crystal Properties*, Vienna University of Technology, Vienna, Austria, (2001)

[33] P. Hohenberg, W. Kohn, Phys. Rev. 136 (3B) (1964) B864

[34] J.P. Perdew, S. Burke, M. Ernzerhof, Phys. Rev. Lett. 77, (1996) 3865.

[35] F. Tran, P. Blaha, K. Schwarz, J. Phys. Condens. Matter 19 (19) (2007) 196208

[36] Monkhorst, H. J.; Pack, J. D. Phys. Rev. B (1976) 13, 5188

[37] A. Zunger, S.H. Wei, L.G. Ferreira, J.E. Bernard, Phys. Rev. Lett. 65 (1990) 353

[38] S. Azzi, A. Zaoui, H. Boublenza, I. S. Messaoudi, and M. Ferhat. J. ALLOY. COMPD. (2014) 588, 133

[39] A. D. Becke, E. R. Johnson, J. Chem. Phys. (2012) 124, 221101

[40] F.D. Murnaghan, Proc. Nat. Acad. Sci. USA. (1944) 30, 5390

[41] A. Baida, , M. Ghezali. Comput. Condens. Matter. (2018) 17, e00333

[42] A. Bouhemadou, R. Khenata, M. Kharoubi, T. Seddik, A.H. Reshak, Y.A. Douri, Comput. Mater. Sci. (2009) 45, 474

[43] O. Madelung. Landolt-BÖrnstein, Semiconductors, Physics of Group IV Elements and III–V Compounds New Series, (1982) vol. 17, Springer-Verlag, Berlin

[44] O. Arbouche, B. Belgoumene, B. Soudini, Y. Azzaz, H. Bendaoud, K. Amara, Comput. Mater. Sci. (2010) 47, 685

[45] W. Zhang, W. Wu, X. Cheng, Physica B. (2010) 05, 4536.

[46] M.I. McMahon, R.J. Nelmes, N.G. Wright, D.R. Allan, in: Proceedings of the Joint Conference of the AIRAPT/APS on High-Pressure Science and Technology, (1993)

[47] C.S. Menoni, I.L. Spain, Phys. Rev. B (1987) 35, 7520

[48] S. Minomura, H.G. Drickamer, J. Phys. Chem. Solids. (1962) 23, 451

[49] J.C. Jamieson, Science. (1963) 139, 762

[50] A. Mujica, R.J. Needs, Phys. Rev. B. (1997) 55, 9659

[51] M. Jamal. *A Package for Calculating Elastic Tensors of Cubic Phases by Using Second-order Derivative with Wien2k Package*

[52] D.C. Wallace, *Thermodynamics of crystals*, Willey, NewYork, (1972)

[53] D. N. Nichols, D. S. Rimai, and R. J. Sladek, Solid State Commun. (1980) 36, 667

[54] R. Weil and W. O. Groves, J. Appl. Phys. (1968) 39, 4049

[55] Wang, S. Q., & Ye, H. Q. Phys. Status. Solidi (b). (2003) 240(1), 45-54

[56] A. Bouhemadou. Comput. Mater. Sci. (2008) 43(4), 1112

[57] P. Rochon, E. Fortin, Phys. Rev. B12n (1975) 5803

[58] M. Yousaf, M.A. Saeed, R. Ahmed, Commun. Theor. Phys. 58, (2012) 777

[59] R.A. Swalin, *Thermodynamics of Solids*, 2nd ed., Series on the Science and Technology of Material, Wiley, New York, (1972)

[60] A Briedi, thesis,*Temperature-pressure phase diagrams, structural and electronic properties of binary and pseudobinary semiconductor: an ab initio study*, VERLAINE-METZ University, (2011)

[61] PY. Yu and M. Cardona, *Fundamental of semi-conductors: physics and materials properties,* 4thedt. Springer-Verlag, Berlin and Heidelberg, (1996)

[62] I.Gorczyca, N.E. Christensen, M. Alouani.. Phys. Rev. B, 39(11), (1989) 7705

[63] M. Nishiwaki, H. Fujiwara, Comput. Mat. Sci.172. (2020) 109315

[64] S. O. KASAP, *Principal of electronic materials and devices*, fourth ed., McGraw-Hill Education, (2018)

[65] L. Yu and A. Zunger, Phys. Rev. Lett., (2012) 108, 068701

[66] M.A. Green et. all, Solar cell efficiency tables (version 56), Prog. Photovolt. Res. Appl. (2020) 28, 629–638

[67] P. Singh and N.M. Ravindra. Solar Energy Materials & Solar Cells 101, (2012) 36–45

[68] M.A. Green, *Solar Cells*, Prentice-Hall, Englewood Cliffs, NJ, (1982)

[69] D. E. Aspnes and A. A. Studna, Phys. Rev. B 27, (1983) 985

[70] C. M. Herzinger et all., J. Appl. Phys. 77 (1995)1715